bioRxiv preprint doi: https://doi.org/10.1101/2023.05.15.540780; this version posted May 16, 2023. The copyright holder for this preprint (which was not certified by peer review) is the author/funder, who has granted bioRxiv a license to display the preprint in perpetuity. It is made available under aCC-BY-NC-ND 4.0 International license.

Direct detection of deformation modes on varying length scales in active biopolymer networks

Samantha Stam[1,2,3,4], Margaret L. Gardel[2,5,6], Kimberly L. Weirich[5,7]

[1]Biophysical Sciences Graduate Program, University of Chicago, Chicago, IL 60637
[2]Institute for Biophysical Dynamics, University of Chicago, Chicago, IL 60637
[3]Department of Oncological Sciences, University of Utah, Salt Lake City, UT 84112
[4]Huntsman Cancer Institute, University of Utah, Salt Lake City, UT 84112
[5]James Franck Institute, University of Chicago, Chicago, IL 60637
[6]Department of Physics, University of Chicago, Chicago, IL 60637
[7]Department of Materials Science & Engineering, Clemson University, Clemson, SC 29634

Correspondence: samantha.stam@hci.utah.edu, gardel@uchicago.edu, weirich@clemson.edu

ABSTRACT

Correlated flows and forces that emerge from active matter orchestrate complex processes such as shape regulation and deformations in biological cells and tissues. The active materials central to cellular mechanics are cytoskeletal networks, where molecular motor activity drives deformations and remodeling. Here, we investigate deformation modes in actin networks driven by the molecular motor myosin II through quantitative fluorescence microscopy. We examine the deformation anisotropy at different length scales in networks of entangled, cross-linked, and bundled actin. In sparsely cross-linked networks, we find myosin-dependent biaxial buckling modes across length scales. In cross-linked bundled networks, uniaxial contraction is predominate on long length scales, while the uniaxial or biaxial nature of the deformation depends on bundle microstructure at shorter length scales. The anisotropy of deformations may provide insight to regulation of collective behavior in a variety of active materials.

bioRxiv preprint doi: https://doi.org/10.1101/2023.05.15.540780; this version posted May 16, 2023. The copyright holder for this preprint (which was not certified by peer review) is the author/funder, who has granted bioRxiv a license to display the preprint in perpetuity. It is made available under aCC-BY-NC-ND 4.0 International license.

INTRODUCTION

Active materials are ubiquitous in biology and of increasing interest in engineered materials due to their emergent collective behavior and responsive properties, such as correlated motion, large density fluctuations, and directed force transmission (*1*). These intriguing materials are made of mechanically active building blocks that exert internal forces and produce local motion, resulting in emergent collective phenomena. In biology, active materials emerge from collections of active particles at various length scales, including flocks of birds, suspensions of swarming bacteria, layers of motile cells, and networks of polymers, while engineered active matter includes collections of chemically reactive colloids and mechanically driven particles (*2*). Developing a fundamental understanding of the mechanical properties that emerge from active material microstructure is necessary to characterize functions such as roles within biological tissues and potential for engineered applications.

In biological cells, active materials comprise the cytoskeleton, networks and bundles of filament-forming proteins such as actin and microtubules. A primary way that the cytoskeleton is made active is through molecular motors, such as myosin II, that translate the chemical energy of nucleotide hydrolysis into forces that drive filament motion and deformation in actin networks. Myosin II motor heads take force-generating steps, while interacting with multiple actin filaments, resulting in actin filament sliding and buckling that leads to overall network deformation. The activity of motors can also drive relative sliding of filaments and gather filament ends into central locations in a process known as polarity sorting (*3*-*6*).

These cytoskeletal materials exhibit classic active matter characteristics such as correlated motion (*7, 8*) and large density fluctuations (*7*). However, in contrast to many other active materials, the constituent particles in the cytoskeleton are filaments that are highly deformable and polar, resulting in deformations that depend on orientation and mechanical properties of the filament. For example, actin filaments are semi-flexible polymers, giving rise to an asymmetry in a filament's response to compression relative to extension. This asymmetric mechanical response leads to actin filaments preferentially buckling under load, and is hypothesized to be critical to producing the net contractile behavior characteristic of active cytoskeletal networks (*9*-*13*). Previous experimental and theoretical studies have suggested that the types of network deformation modes, buckling and sliding, are regulated through the network microstructure and activity such as filament rigidity (*14*), cross-linking between filaments (*12, 14*-*17*), or motor concentration and properties (*10, 12, 18*). These deformation modes underlie differences in emergent network properties, including whether the material is predominately contractile or extensile. To understand the microscopic origin of the active material behavior, most previous experimental studies have relied on indirect assessment of deformation modes via comparison of contraction rate or other metrics to theoretical models (*15, 16*).

Here, we investigate how active network deformation modes depend on length scale and internal stress through quantitative image analysis of deformation anisotropy (*14*) in cytoskeletal networks with different microstructures. We find that uniaxial deformations, which indicate actin filament sliding (*14*), are the predominate deformation mode in networks of semi-flexible actin at sufficiently low internal stress. At higher myosin densities, the internal stress increases, leading to length-scale dependent biaxial buckling

bioRxiv preprint doi: https://doi.org/10.1101/2023.05.15.540780; this version posted May 16, 2023. The copyright holder for this preprint (which was not certified by peer review) is the author/funder, who has granted bioRxiv a license to display the preprint in perpetuity. It is made available under aCC-BY-NC-ND 4.0 International license.

deformations. At intermediate myosin densities, long-wavelength buckling deformations continually rearrange the network persist for tens of minutes without causing network clustering typically observed at higher densities (*11, 19-21*). In networks of cross-linked rigid bundles, by contrast, we observe different patterns of deformation as a function of internal stress and length scale than in networks of filaments. Networks of bundles deform uniaxially on sufficiently large length scales. However, bundles can have different microstructures, where filaments are aligned with the same polarity or with randomly oriented filaments. We find that these different bundle microstructures exhibit either stress-independent (aligned bundles) or stress and length-scale dependent deformation modes (random bundles). These results reveal how active materials tune deformations at different length scales with microstructure and internal force, emphasizing the importance of considering length scale in building physical models.

METHODS

Protein purification, fluorescent labeling, and storage

Actin, skeletal muscle myosin II, filamin, fascin, and fimbrin were purified as described previously and stored as frozen stocks at -80°C (*14, 22, 23*). Actin was purified from rabbit acetone powder (Pel-Freez Biologicals) and stored 2 mM Tris·HCl, pH 8.0, 0.2 mM ATP, 0.2 mM $CaCl_2$, 0.2 mM DTT, and 0.005% NaN_3 (*24*). Myosin II was prepared from fresh chicken skeletal muscle 5 mM PIPES, pH 7.0, 450 mM KCl (*25*). Filamin was purified from chicken gizzard and stored in 10 mM Tris-HCl, pH 7.4, 120 mM NaCl, 0.5 mM EGTA, 1 mM DTT (*26*). Human fascin (GST tag fusion) and pombe fimbrin (HisTag fusion) were purified from E. coli using plasmids from D. Kovar Lab (University of Chicago) (*27, 28*). Actin and myosin II were fluorescently labeled with tetramethylrhodamine-6-maleimide (TMR, Life Technologies) and Alexa-647 maleimide (Life Technologies), respectively (*29*).

Sample preparation

To prepare microscopy samples, a chamber was constructed from a coverslip passivated with an oil-surfactant layer or lipid bilayer. To prepare an oil-surfacant passivated sample chamber, PFPE-PEG-PFPE surfactant (008; RAN Biotechnologies) was dissolved in a fluorinated oil (Novec-7500 Engineered Fluid; 3M) at a concentration of 2 wt% (*8*). Coverslips (no. 1.5, Fisherbrand) were cleaned by sonication and rinsed in pure water and ethanol. Coverslips were then treated to make hydrophobic by incubating in a 2% vol/vol solution of triethoxy(octyl)silane (440213; Sigma-Aldrich) in isopropanol. The hydrophobic coating was removed from entire coverslip surface except for a 2 mm x 2 mm square region by exposing to UV-ozone for 10 minutes with a square Teflon mask covering the region. This constrained the oil to the square region and prevented flow generated by seeping at the coverslip edges. A glass cylinder was epoxied to the coverslip to produce a microscopy chamber. A minimal volume of oil (~ 3.5 µL) was added to the chamber to coat the surface, and excess solution removed immediately prior to adding the actin polymerization mixture.

To prepare a lipid bilayer passivated sample chamber (*30*), coverslips (no. 1.5; Fisherbrand) were first rinsed with water and ethanol then cleaned through exposure to UV-ozone for 20 min. A glass cylinder was epoxied to the clean coverslip, and vesicle

bioRxiv preprint doi: https://doi.org/10.1101/2023.05.15.540780; this version posted May 16, 2023. The copyright holder for this preprint (which was not certified by peer review) is the author/funder, who has granted bioRxiv a license to display the preprint in perpetuity. It is made available under aCC-BY-NC-ND 4.0 International license.

buffer (10 mM sodium phosphate, pH 7.5, and 140 mM NaCl) added as soon as possible. DOPC vesicles (1,2-dioleoyl-sn-glycero-3-phosphocholine; Avanti Polar Lipids) were then added to a concentration of 100 μM. The coverslip was incubated with the vesicles for 15 min to allow bilayer formation, before the bilayer was rinsed with a buffer comprising of 1x F-buffer (below, in actin polymerization) prior to adding the final sample.

Unbundled actin networks

To prepare cross-linked actin networks crowded to a coverslip surface (*11*), a mixture of 0.3 wt% 15 cp methylcellulose, 1 μM actin (1:10 TMR-maleimide labeled:unlabeled), 0.002 μM filamin crosslinker, and an oxygen scavenging system to prevent photobleaching [4.5 mg/mL glucose, 2.7 mg/mL glucose oxidase (345486; Calbiochem), 1,700 units/mL catalase (02071; Sigma), and 0.5 vol/vol % β-mercaptoethanol], was made in 1x F-buffer (10 mM imidazole, pH 7.5, 1 mM MgCl2, 50 mM KCl, 0.2 mM EGTA, and 4 mM ATP). Actin was allowed to polymerize and crowd to the coverslip surface for 30 minutes before addition of dimeric Alexa-647 labeled myosin.

Bundled actin networks

Bundled actin networks were constructed similarly to unbundled networks, but have no cross-linker (filamin) during the initial 30 min polymerization period. To prepare fascin cross-linked bundles, fascin was added at a ratio of 1:10 fascin:actin to the polymerized actin sample and incubated for 20 minutes to allow bundle formation. For additional filamin cross-linking, filamin was subsequently added at a ratio of 1:500 filamin:actin and incubated for an additional 20 minutes. For fimbrin bundles, the fimbrin was added 20 minutes after actin polymerization at a ratio of 1:10 and incubated for 20 minutes. Myosin filaments were polymerized separately for 10 minutes in the same buffer conditions described above for actin polymerization before addition to the bundled actin networks.

Image acquisition and analysis

An inverted microscope (Eclipse Ti-E; Nikon) with a spinning-disk confocal head (CSU-X; Yokagawa Electric) was used for all imaging. Imaging was done under magnification of a 40× 1.15 N.A. water-immersion objective (Apo LWD; Nikon) or a 60×/1.49 NA oil immersion objective (Zeiss). Images were acquired with a CMOS camera (Zyla-4.2-USB3; Andor) or a CCD camera (Coolsnap HQ2, Photometrics). Images were acquired every 1 s for Figs. 1-5 and every 5 s for Fig. 6. Calculation of flow vectors and deformation anisotropy was conducted as we described previously (*14*) using PIV software (www.oceanwave.jp/softwares/mpiv/) and custom Matlab scripts. Values of ρ_{myo} and $P_{biaxial}$ were smoothed such that data points report the average value over overlapping windows of 50 s in Fig. 6 and 20 s in all other figures.

RESULTS

To create a cytoskeletal material inspired by the cellular cortex, we crowd actin filaments to a thin, dense layer with a depletion agent (see Methods) (*11*). Filamin, an actin cross-linking protein, connects entangled filaments into networks without causing bundling when incorporated at a low concentration (0.01 μM; 1:100 molar ratio with

bioRxiv preprint doi: https://doi.org/10.1101/2023.05.15.540780; this version posted May 16, 2023. The copyright holder for this preprint (which was not certified by peer review) is the author/funder, who has granted bioRxiv a license to display the preprint in perpetuity. It is made available under aCC-BY-NC-ND 4.0 International license.

respect to actin monomer) (Fig. 1A). A thin oil-surfactant layer passivates the coverslip surface against protein adhesion (*8*). To introduce activity, we add myosin II dimers. We define the time the motors are first added to the sample as time t = 0 s. Upon dilution in the sample buffer, which contains lower salt concentration than the storage buffer, the myosin II dimers polymerize into puncta (referred to as myosin, Fig. 1B, white puncta), which are filaments that each contain several hundred myosin II motors (*11*).

Network deformation mode anisotropy depends on myosin

Myosin incorporates into the network, initially increasing from 0 to 0.05 puncta/μm^2 over the first ~100 s, as myosin polymerizes into elongated puncta that bind to actin filaments (Fig. 1C). During this initial period of myosin accumulation, there is an increase in the fluctuations along the contour of actin filaments, indicating myosin-induced stresses bending actin filaments. This filament bending induces local filament rearrangement without substantially changing network density (Fig. 1B, 1:15-2:55). As myosin continues to accumulate, the network begins to contract, with actin filaments and myosin rearranging into clusters with a central myosin core (Fig. 1B, 0:00 and 0:50), eventually forming voids and separated clusters (Fig. 1B, 5:00). This clustering is consistent with previous reports of actomyosin network contraction *in vitro*, where dense actomyosin clusters form given a sufficiently high myosin concentration (*11, 19-21*). Concomitant with clustering, the number density of myosin puncta begins to decrease near t = 100 s (Fig. 1C).

To characterize the anisotropy of the network deformation, we use the flow dipole moment tensor (*14*). Briefly, we first characterize the local actin flow in the network through calculating the local displacement vectors between frames using Particle Imaging Velocimetry (PIV, see Methods). To do this, we split each image into non-overlapping boxes with length s and define the position vector, $\vec{r}$, as the vector from the center of a box to the location of an enclosed PIV vector. From these vectors, we calculate the flow dipole moment tensor:

$$M_{ij} = \sum_{\vec{r}} v_{act}(\vec{r})_i r_j \quad (1)$$

where $\vec{v}_{act}$ is a local PIV vector. Diagonalization of this tensor yields the principal deformation axes as well as the eigenvalues, M_{min} and M_{max}, which characterize the local deformation anisotropy (Fig. 2A). A value of M_{min}/M_{max} of 0 indicates that the deformation of actin network within the defined box is along a single axis. At the other extreme, a value of M_{min}/M_{max} of 1 indicates that the deformation is completely biaxial.

To visualize the anisotropy of deformations, we superimpose ellipses on the actin images, where each ellipse has major and minor axes with magnitude M_{min} and M_{max}, respectively (Fig. 2B). For s = 20 μm, the magnitudes of M_{min} and M_{max}, and so the size of the representative ellipses, increases between time 0:00 to 1:40 (Fig. 2B), indicating an increase in extent of deformation as myosin accumulates in the network. To probe the deformation anisotropy at different length scales, we vary the box length, s. At a smaller

bioRxiv preprint doi: https://doi.org/10.1101/2023.05.15.540780; this version posted May 16, 2023. The copyright holder for this preprint (which was not certified by peer review) is the author/funder, who has granted bioRxiv a license to display the preprint in perpetuity. It is made available under aCC-BY-NC-ND 4.0 International license.

length scale, s = 5 μm, we find that M_{min} and M_{max} increase as myosin accumulates similarly to s = 20 μm.

The deformation anisotropy also changes as the network reorganizes. Deformations are predominantly uniaxial when myosin density in the network is initially low (left panels in Fig. 2B and 2D, quantified in Fig. 2C and 2E, blue curves). This is in contrast to our previously reported data of networks with greater initial myosin density, which exhibited biaxial deformation modes arising from filament buckling (*14*). As network deformation proceeds, corresponding to increased myosin accumulation, we observe a large shift in the probability distribution of M_{min}/M_{max} at s = 20 μm such that the distribution becomes peaked at M_{min}/M_{max} ~ 0.8 (Fig. 2C). At a smaller length scale (s = 5 μm, Fig. 2E), the distribution also shifts to more biaxial deformations after the addition of myosin, but distribution of M_{min}/M_{max} remains more uniaxial at all times and the changes over time are smaller. At long times on both length scales, the distribution eventually shifts back to a distribution with fewer biaxial deformations. The deformation anisotropy is therefore strongly dependent on changes to myosin density (and presumed internal force) and/or structural changes in the network.

Small-wavelength biaxial deformations require higher internal stress than long-wavelength modes and precede myosin clustering

To examine how biaxial deformations are correlated with changes in the network internal force or microstructure, we quantify changes in the number of biaxial deformations during the myosin accumulation and clustering stages. We define $P_{biaxial}(s)$ as the proportion of deformations in the network at a given time with M_{min}/M_{max} values greater than 0.5. We monitor changes in $P_{biaxial}(s)$ (Fig. 3A, symbols) during accumulation and decrease in myosin puncta density (Fig. 3A, solid line, normalization of data from Fig. 1B). $P_{biaxial}(s)$ is initially constant over a range of low myosin density, but sharply increases above a threshold myosin density. Significantly, the peak in $P_{biaxial}(s)$ for both s = 5-10 μm s = 45-50 μm occurs near the maximum myosin puncta density at t = 105 s.

We then examine how biaxial deformation modes of varying length scales depend increasing internal stress, by focusing on the period of initial myosin accumulation in the network, prior to significant network reorganization. Comparing $P_{biaxial}$ from two length scale ranges, s = 5-10 μm (Fig. 3B, yellow) and 45-50 μm (Fig. 3B, black), we find that $P_{biaxial}(s)$ is consistently lower for smaller values of s, regardless of the amount of myosin puncta. At both length scales, a sharp increase of $P_{biaxial}(s)$ occurs at a threshold myosin density. The initial increase occurs at lower myosin density for the larger values of s. To quantify this, we define a critical myosin density, $\rho_{activate}$, required to raise $P_{biaxial}(s)$ by 20% of its baseline value (dotted lines, Fig. 3B). We can quantify the increase in biaxial deformation modes through $\Delta P_{biaxial}(s)$, the difference between the value of $P_{biaxial}(s)$ at the peak in myosin puncta density and the average baseline value of $P_{biaxial}(s)$ at low density (Fig. 3C). This quantity increases sharply from small (5-10 μm) to intermediate (15-20 μm) length scales and is maximal at 25-30 μm before decreasing slightly at the longer length scales (> 35 μm). The dependence of the increase in biaxial deformations

bioRxiv preprint doi: https://doi.org/10.1101/2023.05.15.540780; this version posted May 16, 2023. The copyright holder for this preprint (which was not certified by peer review) is the author/funder, who has granted bioRxiv a license to display the preprint in perpetuity. It is made available under aCC-BY-NC-ND 4.0 International license.

on length scale indicates a greater force required to induce buckling deformations at shorter length scales.

Lower myosin densities do not induce network clustering (*19, 20*) and the deformations leading to network structural change (*18*). To further explore the requirements for biaxial modes, we reduce the concentration of myosin further (by how much?). Similar to the samples with higher myosin concentration (Fig. 1), bending of actin filaments occurs after the addition of myosin (Fig. 4A). However, even after 20 minutes of network rearrangement, we do not observe dense clusters or opening of voids in the network. Some clustering of myosin occurs, but on a much longer time scale as is indicated by the decrease of myosin puncta density at $t \sim 700$ s (Fig. 4B, red line).

Similar to the network with higher myosin density, a sharp increase in biaxial deformations at s = 45-50 μm occurs during the myosin increase (Fig. 4B, yellow circles). By contrast, only small changes occur at the shortest length scale (s = 5-10 μm) investigated. Intriguingly, $P_{biaxial}(s)$ reaches a plateau at both values of s in the low myosin sample (Fig 4B) after the myosin puncta density begins to decrease rather than decreasing as observed in the higher myosin sample (Fig. 3A). Plotting $P_{biaxial}(s)$ for s = 5-10 μm and s = 45-50 μm against myosin density during accumulation (Fig. 4C) reveals similar baseline values at $\rho_{myo} < 0.001$ μm^{-2} as the data from Fig 3B, but smaller increases in $P_{biaxial}(s)$. This pattern is confirmed by measuring $\Delta P_{biaxial}(s)$ across a range of length scales in Fig. 4D, where all values of $\Delta P_{biaxial}(s)$ are smaller than their counterparts in Fig. 3C.

To determine whether activation of biaxial modes at smaller length scales consistently requires more internal stress, we measure the average density of myosin required to raise $P_{biaxial}(s)$ by 20 percent of its baseline value during myosin polymerization ($\rho_{activate}(s)$, indicated by dotted lines in Fig. 3B) in five independent samples (Fig 5E). We observe that $\rho_{activate}(s)$ decreases monotonically with increasing s. These data indicate that networks with insufficient internal stress to significantly activate modes with $s < 10$ μm but sufficient stress to activate longer wavelength modes can continually rearrange without network cluster formation or decline in buckling modes for 20 minutes or more.

The frequency of biaxial and uniaxial deformations in networks of polar, rigid bundles is stress-independent

We previously found that cross-linked networks of rigid bundles contract via uniaxial deformations arising from relative sliding of the bundles (*14*). We now build on these findings to examine the length scale and force dependence of these deformations. Like our previous study, networks are constructed with two different actin cross-linkers. One type of cross-linker, fascin, links actin filaments together into bundles with a uniform polarity (*31*) (Fig. 5A). We observe that these bundles appear as straight rod with diffraction limited width that may overlap with other bundles (Fig. 5A, Fig. 5B). We add second type of cross-linker which is flexible, filamin, after the fascin-mediated bundles form to ensure that the bundles form an inter-connected network. Effectively, the bundles act as polar filaments with a higher stiffness than the unbundled, semi-flexible actin in the previous sections (*22*).

bioRxiv preprint doi: https://doi.org/10.1101/2023.05.15.540780; this version posted May 16, 2023. The copyright holder for this preprint (which was not certified by peer review) is the author/funder, who has granted bioRxiv a license to display the preprint in perpetuity. It is made available under aCC-BY-NC-ND 4.0 International license.

Networks bundled with fascin and cross-linked with filamin form asters upon addition of myosin (Fig. 5B, (*32*)). As with the unbundled network in Fig. 1, the density of myosin puncta initially increases as myosin accumulates in the network, and then decreases as clusters form (Fig 5C, solid red line (*14*)). Also similar to the previous networks, the magnitude of the flow dipole deformation ellipses increases after myosin addition (Fig. 5D). However, the ellipses remain more uniaxial over the course of network rearrangement, with the values of $P_{biaxial}(s)$ at both s = 5-10 μm and s = 45-50 μm remaining less than 0.4 (Fig. 5C, symbols). The magnitude of $P_{biaxial}(s)$ is larger at s = 45-50 μm than s = 5-10 μm in Fig. 5C, consistent with the network being increasingly anisotropic as the length scale decreases to approach that of a single bundle. Changes in $P_{biaxial}(s)$ at both length scales during both the myosin increase and decrease are much smaller than their counterparts in Fig. 3A and Fig. 4B. Notably, the sharp increase in $P_{biaxial}(s)$ due to buckling is not observed. In Fig. 5E, we measure the change in $P_{biaxial}(s)$ between the initial myosin addition and the maximum of myosin puncta density for a range of s. A very small change in $P_{biaxial}(s)$ is observed across the entire range from 5 to 50 μm. Together, these data indicate that uniaxial deformations are robust within the network of rigid, polar bundles at a variety of length scales and internal stress magnitudes.

$P_{biaxial}(s)$ may change in opposite directions at different values of s

To more broadly understand the influence of actin bundle structure on network deformation modes, we use a different rigid actin cross-linker, fimbrin, to make actin bundles which have similar packing of the actin filaments as fascin bundles (*33*), but with filaments that are aligned with random polarity (Fig. 6A) (*34*). Myosin filaments can simultaneously bind to actin filaments with opposite polarity and build internal stress within a bundle (*22*). Myosin activity induces fimbrin-bundled networks to coarsen into dense actomyosin clusters (Fig. 6B), similar to the fascin-bundled networks. However, the intermediate stages of network reorganization are distinct from the polar bundles formed by fascin. While the fascin bundles appear rigid, in fimbrin bundled actin, there is visual evidence of buckling or bending of bundles (Fig. 6B, second and third panels). Closer examination reveals angular buckles flanked by regions that remain straight (Fig. 6C). In some regions, biaxial flow dipole ellipses are observed near buckles at small s (Fig. 6D, top panel), while the overall ellipse at larger s is uniaxial (Fig. 6D, bottom panel).

Changes in network deformation modes are reflected by an increase in $P_{biaxial}(s)$ at s = 3-6 μm upon addition of myosin followed by a plateau and slight decrease at long times (Fig. 6E). At a larger value of s (39-42 μm, Fig. 6E), $P_{biaxial}(s)$ fluctuates during network reorganization. To understand the stress dependence of these behaviors, we plot $P_{biaxial}(s)$ as a function of myosin density during myosin puncta accumulation in Fig. 6F. During the stress buildup phase, a baseline value of $P_{biaxial}(s)$ occurs at s = 3-6 μm at $\rho_{myo} < 0.02$ μm^{-2} before a sharp increase of $P_{biaxial}(s)$. This is qualitatively similar to the increase in $P_{biaxial}(s)$ in unbundled neworks due to buckling. At the larger length scale of s = 39-42 μm, a slight increase in $P_{biaxial}(s)$ above the baseline occurs at a lower value of ρ_{myo} than the $P_{biaxial}(s)$ increase occurring at s = 3-6 μm. However, a decrease in $P_{biaxial}(s)$ soon follows at a higher value of ρ_{myo}, and $P_{biaxial}(s)$ dips below its baseline value. Interestingly, this decrease occurs at approximately the same value of ρ_{myo} as the

bioRxiv preprint doi: https://doi.org/10.1101/2023.05.15.540780; this version posted May 16, 2023. The copyright holder for this preprint (which was not certified by peer review) is the author/funder, who has granted bioRxiv a license to display the preprint in perpetuity. It is made available under aCC-BY-NC-ND 4.0 International license.

increase in $P_{biaxial}(s)$ at s = 3-6 μm (~0.03 μm^{-2}). Finally, we examine the change in $P_{biaxial}(s)$ from its baseline at low myosin to its extremum during myosin accumulation at varying s to further understand the length scale dependence (Fig. 6G). Most of the $\Delta P_{biaxial}(s)$ values at s = 30 μm or less are slightly positive, while a decrease to negative values occurs at s > 33 μm. Together, these data underscore the importance of measuring $P_{biaxial}(s)$ at varying s for a more complete understanding of network deformation modes.

DISCUSSION

Deformations in active, soft materials are critical during processes requiring changes of material shape, size, or transport of components. The mode of deformation at the microscale can include both translocation of components with respect to one another and deformation of components, regulating material scale mechanical response, such as contraction or expansion (*12*), flow-induced transport (*8, 35*), or force transmission to external physical attachments such as cellular adhesions. To understand how microscopic material structure influences deformations and mechanical response, substantial efforts have been made connecting theoretical and computational models of material deformation to available experimentally observable quantities (*36*). Here, we build on our previous work in which deformation anisotropy was analyzed at a single length scale to identify actin buckling and sliding (*14*) to bridge the gap between experiments in which deformation modes typically must be inferred from indirect measurements and modeling in which the deformations on all length scales are directly accessible.

In cells, microscale deformations critical to cellular scale processes occur within a crowded and complex environment including protein filaments and large lipid-based organelles such as mitochondria and the endoplasmic reticulum. Our analysis may readily be extended to examine spatiotemporal correlations between deformations in different components of such composite materials. This research is a step toward understanding how forces are transmitted in these complex, active materials. For example, recent research has indicated that organelle-organelle contacts are tethers (*37*) potentially capable of exerting forces to divide mitochondria (*38*), suggesting that force transmission occurring at these sites may be important for maintaining normal organelle structure and distribution. Mechanosensitive processes, such as the opening of ion channels, may also be related to deformations in cells and in the fibrous networks of the extracellular matrix (*39*). Force transmission also occurs between different components of the cytoskeleton, with microtubules potentially becoming bent or broken in response to contractile forces generated by actin networks (*40, 41*). Deformation mode analysis of both networks simultaneously has the potential to inform underlying mechanisms of these and other physiological processes, such as cell migration. Additionally, altering the physical structure of mitochondria via deformation and translocation may influence their metabolism (*42*) and, consequently, their ability to produce energy or induce detrimental effects that lead to cell aging or death. While protein-based devices (*43*) lack the longevity of other artificial materials, there is interest in using the design principles of biology to

bioRxiv preprint doi: https://doi.org/10.1101/2023.05.15.540780; this version posted May 16, 2023. The copyright holder for this preprint (which was not certified by peer review) is the author/funder, who has granted bioRxiv a license to display the preprint in perpetuity. It is made available under aCC-BY-NC-ND 4.0 International license.

engineer materials with similar properties. For example, the mechanisms by which cell deformations are tunable can be elucidated via modifying their protein content or physical linkages between components, such as artificially induced organelle-organelle contacts, (*44, 45*). Better understanding these materials will allow for complex mechanical responses in biological materials to be modified or mimicked in bio-inspired soft materials.

ACKNOWLEDGEMENTS

We thank members of David Kovar's laboratory, particularly J. Christensen, J. Winkelman, and C. Suarez, for the purified protein cross-linker fimbrin, as well as the construct for fascin and advice on purifying proteins. This research was partially supported by the University of Chicago MRSEC, funded through the National Science Foundation award DMR-2011854. This research was also supported in part by the National Science Foundation EPSCoR Program under NSF Award # OIA-1655740 and the National Institutes of Health National Institute of Biomedical Imaging and Bioengineering Training grant number T32EB009412.

REFERENCES

1. G. Gompper *et al.*, The 2020 motile active matter roadmap. *Journal of Physics: Condensed Matter* **32**, 193001 (2020).
2. M. C. Marchetti *et al.*, Hydrodynamics of soft active matter. *Reviews of Modern Physics* **85**, 1143 (2013).
3. F. J. Nedelec, T. Surrey, A. C. Maggs, S. Leibler, Self-organization of microtubules and motors. *Nature* **389**, 305-308 (1997).
4. R. Urrutia, M. A. McNiven, J. P. Albanesi, D. B. Murphy, B. Kachar, Purified Kinesin Promotes Vesicle Motility and Induces Active Sliding between Microtubules Invitro. *Proceedings of the National Academy of Sciences of the United States of America* **88**, 6701-6705 (1991).
5. V. Wollrab *et al.*, Polarity sorting drives remodeling of actin-myosin networks. *Journal of Cell Science* **132**, jcs219717 (2018).
6. A. Sciortino, A. R. Bausch, Pattern formation and polarity sorting of driven actin filaments on lipid membranes. *Proceedings of the National Academy of Sciences* **118**, e2017047118 (2021).
7. V. Schaller, C. Weber, C. Semmrich, E. Frey, A. R. Bausch, Polar patterns of driven filaments. *Nature* **467**, 73-77 (2010).
8. T. Sanchez, D. T. Chen, S. J. DeCamp, M. Heymann, Z. Dogic, Spontaneous motion in hierarchically assembled active matter. *Nature* **491**, 431-434 (2012).
9. T. B. Liverpool, M. C. Marchetti, J. F. Joanny, J. Prost, Mechanical response of active gels. *EPL (Europhysics Letters)* **85**, 18007 (2009).
10. M. Lenz, T. Thoresen, M. L. Gardel, A. R. Dinner, Contractile Units in Disordered Actomyosin Bundles Arise from F-Actin Buckling. *Physical Review Letters* **108**, (2012).
11. M. P. Murrell, M. L. Gardel, F-actin buckling coordinates contractility and severing in a biomimetic actomyosin cortex. *Proceedings of the National Academy of Sciences of the United States of America* **109**, 20820-20825 (2012).
12. J. M. Belmonte, M. Leptin, F. Nédélec, A theory that predicts behaviors of disordered cytoskeletal networks. *Mol Syst Biol* **13**, 941 (2017).

bioRxiv preprint doi: https://doi.org/10.1101/2023.05.15.540780; this version posted May 16, 2023. The copyright holder for this preprint (which was not certified by peer review) is the author/funder, who has granted bioRxiv a license to display the preprint in perpetuity. It is made available under aCC-BY-NC-ND 4.0 International license.

13. P. Ronceray, C. P. Broedersz, M. Lenz, Fiber networks amplify active stress. *Proceedings of the National Academy of Sciences* **113**, 2827-2832 (2016).
14. S. Stam *et al.*, Filament rigidity and connectivity tune the deformation modes of active biopolymer networks. *Proceedings of the National Academy of Sciences* **114**, E10037 (2017).
15. H. Ennomani *et al.*, Architecture and Connectivity Govern Actin Network Contractility. *Curr Biol* **26**, 616-626 (2016).
16. K. T. Stanhope, V. Yadav, C. D. Santangelo, J. L. Ross, Contractility in an extensile system. *Soft Matter* **13**, 4268-4277 (2017).
17. R. Blackwell *et al.*, Microscopic origins of anisotropic active stress in motor-driven nematic liquid crystals. *Soft Matter* **12**, 2676-2687 (2016).
18. M. Murrell, M. L. Gardel, Actomyosin sliding is attenuated in contractile biomimetic cortices. *Molecular Biology of the Cell* **25**, 1845-1853 (2014).
19. M. Soares e Silva *et al.*, Active multistage coarsening of actin networks driven by myosin motors. *Proceedings of the National Academy of Sciences of the United States of America* **108**, 9408-9413 (2011).
20. F. Backouche, L. Haviv, D. Groswasser, A. Bernheim-Groswasser, Active gels: dynamics of patterning and self-organization. *Phys Biol* **3**, 264-273 (2006).
21. S. Koehler, V. Schaller, A. R. Bausch, Structure formation in active networks. *Nature Materials* **10**, 462-468 (2011).
22. K. L. Weirich, S. Stam, E. Munro, M. L. Gardel, Actin bundle architecture and mechanics regulate myosin II force generation. *Biophys J* **120**, 1957-1970 (2021).
23. K. L. Weirich *et al.*, Liquid behavior of cross-linked actin bundles. *Proceedings of the National Academy of Sciences* **114**, 2131-2136 (2017).
24. J. Spudich, S. Watt, Regulation of Rabbit Skeletal Muscle Contraction. 1. Biochemical Studies of Interactions of Tropomyosin-Troponin Complex with Actin and Proteolytic Fragments of Myosin. *Journal of Biological Chemistry* **246**, 4866-& (1971).
25. S. S. Margossian, S. Lowey, Preparation of Myosin and Its Subfragments from Rabbit Skeletal-Muscle. *Methods in Enzymology* **85**, 55-71 (1982).
26. S. Craig, C. Lancashire, J. Cooper, Preparation of Smooth-Muscle Alpha-Actinin. *Methods in Enzymology* **85**, 316-321 (1982).
27. D. Vignjevic, J. Peloquin, G. G. Borisy, in *Regulators and Effectors of Small GTPases: Rho Family*. (Academic Press, 2006), vol. Volume 406, pp. 727-739.
28. C. T. Skau, D. R. Kovar, Fimbrin and tropomyosin competition regulates endocytosis and cytokinesis kinetics in fission yeast. *Curr Biol* **20**, 1415-1422 (2010).
29. A. B. Verkhovsky, G. G. Borisy, Non-Sarcomeric Mode of Myosin-Ii Organization in the Fibroblast Lamellum. *Journal of Cell Biology* **123**, 637-652 (1993).
30. K. Weirich, J. Israelachvili, D. Fygenson, Bilayer Edges Catalyze Supported Lipid Bilayer Formation. *Biophysical Journal* **98**, 85-92 (2010).
31. J. R. Bartles, Parallel actin bundles and their multiple actin-bundling proteins. *Current opinion in cell biology* **12**, 72-78 (2000).
32. S. Stam *et al.*, Filament Rigidity And Connectivity Tune The Deformation Modes Of Active Biopolymer Networks. *bioRxiv*, (2017).
33. A. Bretscher, Fimbrin Is a Cytoskeletal Protein That Crosslinks F-Actin In vitro. *Proceedings of the National Academy of Sciences of the United States of America* **78**, 6849-6853 (1981).
34. C. T. Skau *et al.*, Actin Filament Bundling by Fimbrin Is Important for Endocytosis, Cytokinesis, and Polarization in Fission Yeast. *Journal of Biological Chemistry* **286**, 26964-26977 (2011).
35. N. Kumar, R. Zhang, J. J. de Pablo, M. L. Gardel, Tunable structure and dynamics of active liquid crystals. *Science Advances* **4**, eaat7779.

bioRxiv preprint doi: https://doi.org/10.1101/2023.05.15.540780; this version posted May 16, 2023. The copyright holder for this preprint (which was not certified by peer review) is the author/funder, who has granted bioRxiv a license to display the preprint in perpetuity. It is made available under aCC-BY-NC-ND 4.0 International license.

36. S. Banerjee, M. L. Gardel, U. S. Schwarz, The Actin Cytoskeleton as an Active Adaptive Material. *Annual Review of Condensed Matter Physics* **11**, 421-439 (2020).
37. M. Bohnert, Tether Me, Tether Me Not—Dynamic Organelle Contact Sites in Metabolic Rewiring. *Developmental Cell* **54**, 212-225 (2020).
38. J. R. Friedman *et al.*, ER tubules mark sites of mitochondrial division. *Science* **334**, 358-362 (2011).
39. Y.-C. Chuang, C.-C. Chen, Force From Filaments: The Role of the Cytoskeleton and Extracellular Matrix in the Gating of Mechanosensitive Channels. *Frontiers in Cell and Developmental Biology* **10**, (2022).
40. N. Wang *et al.*, Mechanical behavior in living cells consistent with the tensegrity model. *Proc Natl Acad Sci U S A* **98**, 7765-7770 (2001).
41. C. M. Waterman-Storer, E. D. Salmon, Actomyosin-based retrograde flow of microtubules in the lamella of migrating epithelial cells influences microtubule dynamic instability and turnover and is associated with microtubule breakage and treadmilling. *J Cell Biol* **139**, 417-434 (1997).
42. M. Roy, P. H. Reddy, M. Iijima, H. Sesaki, Mitochondrial division and fusion in metabolism. *Current Opinion in Cell Biology* **33**, 111-118 (2015).
43. H. Jia *et al.*, 3D printed protein-based robotic structures actuated by molecular motor assemblies. *Nature Materials* **21**, 703-709 (2022).
44. K. Qiu *et al.*, Light-activated mitochondrial fission through optogenetic control of mitochondria-lysosome contacts. *Nat Commun* **13**, 4303 (2022).
45. F. Shi *et al.*, Optogenetic Control of Endoplasmic Reticulum–Mitochondria Tethering. *ACS Synthetic Biology* **7**, 2-9 (2018).

bioRxiv preprint doi: https://doi.org/10.1101/2023.05.15.540780; this version posted May 16, 2023. The copyright holder for this preprint (which was not certified by peer review) is the author/funder, who has granted bioRxiv a license to display the preprint in perpetuity. It is made available under aCC-BY-NC-ND 4.0 International license.

FIGURE CAPTIONS

Figure 1: Contraction of a actomyosin network, sparsely cross-linked with filamin as myosin accumulates in the network. (A): Schematic of actin network sparsely cross-linked with the flexible cross-linker filamin. (B): Fluorescence microscopy images of actin network (red) and myosin (white). Myosin is added to the actin sample at 0:00 and subsequently polymerizes into punctate filaments. Scale bar is 10 μm. (C): Myosin filament puncta density, ρ_{myo}, varies over an order of magnitude during myosin filament accumulation and clustering.

Figure 2: Contractile deformations in sparsely cross-linked actin networks are uniaxial or biaxial depending on the time point and the length scale. (A): Particle imaging velocimetry generates vectors describing the local material flow in an actin network. The network images are separated into boxes of side length s, and the deformation anisotropy of each box is quantified using the flow dipole tensor and represented by an ellipse. (B): Deformation anisotropy ellipse images at length scale s = 20 μm. (C): Distributions of the deformation anisotropy, M_{min}/M_{max}, at varying time points with s = 20 μm. (D): Deformation anisotropy ellipse images at s = 5 μm. (E): Distributions of M_{min}/M_{max} with s = 5 μm. Scale bars in (B) and (D) are 10 μm.

Figure 3: Biaxial buckling deformations at longer wavelengths are activated more strongly and at lower threshold myosin densities. (A): Left axis: $P_{biaxial}(s)$, defined as the fraction of M_{min}/M_{max} values greater than 0.5, for s = 5-10 μm (open orange circles) and s = 45-50 μm (open black squares) over time during network contraction. Right axis: myosin puncta density, ρ_{myo}, scaled to fall between 0 and 1. (B): $P_{biaxial}(s)$ as a function of myosin puncta density during the myosin accumulation stage (unshaded portion of (A)) for varying values of s. (C): The change in $P_{biaxial}(s)$ between its baseline value at $\rho_{myo} < 10^{-2}$ μm^{-2} and its value at the peak of ρ_{myo}.

Figure 4: Lowering the myosin density produces an active steady state in which long-wavelength buckling modes are activated and persist. (A): Images of actin (red) and myosin filaments (white) in a network with sufficiently low myosin density to prevent network clustering. Scale bar is 10 μm. (B): $P_{biaxial}$ at two values of the length scale s (left axis, open symbols) over time during changes in myosin puncta density (right axis, solid line, scaled to fall between 0 and 1) (C): $P_{biaxial}(s)$ plotted against myosin puncta density during myosin accumulation (unshaded portion of (B)). (D): The change in $P_{biaxial}(s)$ between its baseline value at $\rho_{myo} < 10^{-2}$ μm^{-2} and its value at the peak of ρ_{myo} (E): $\rho_{activate}$, defined as the threshold myosin puncta density required to raise $P_{biaxial}(s)$ by 20% of its baseline value for a given s, averaged over five samples.

Figure 5: Uniaxial deformations on varying length scales in rigid, unipolar bundle network are myosin density independent. (A): Schematic of a rigid, unipolar bundle network. Unipolar actin bundles are first formed with a rigid, unipolar actin cross-linker (fascin) and then linked together with the flexible cross-linker filamin. (B): Images of actin (red) and myosin (white) in bundled network after addition of myosin at 0:00. (C) $P_{biaxial}$ at two value

bioRxiv preprint doi: https://doi.org/10.1101/2023.05.15.540780; this version posted May 16, 2023. The copyright holder for this preprint (which was not certified by peer review) is the author/funder, who has granted bioRxiv a license to display the preprint in perpetuity. It is made available under aCC-BY-NC-ND 4.0 International license.

of s (left axis, open symbols) and ρ_{myo} scaled between 0 and 1 (right axis, solid line) plotted against time after myosin addition. (D). Images of deformation ellipses in bundled network immediately after myosin addition at 0:00 and at 0:25. (E): The change in $P_{biaxial}(s)$ between its initial value at 0:00 and its value at the myosin puncta density peak. Scale bars in (B) and (D) are 10 μm.

Figure 6: Deformations induced by myosin may be either biaxial or uniaxial in networks of mixed polarity bundles depending on the length scale. (A): Schematic of bundles with random actin polarity formed by the cross-linker fimbrin. (B): Images of actin (red) and myosin (white) in bundled network after addition of myosin at 0:00. Scale bar is 10 μm. (C): Image of an angular buckle forming in an actin bundle within the network during contraction. Scale bar is 2 μm. (D): Deformation ellipses at two different length scales in the same network region have different anisotropies. Scale bar is 10 μm. (E): $P_{biaxial}$ at two value of s (left axis, open symbols) and ρ_{myo} scaled between 0 and 1 (right axis, solid line) plotted against time after myosin addition. (F): $P_{biaxial}(s)$ plotted against myosin puncta density during myosin accumulation (unshaded portion of (B)). (G): The change in $P_{biaxial}(s)$ measured between time 0:00 and its maximum difference from this value.

bioRxiv preprint doi: https://doi.org/10.1101/2023.05.15.540780; this version posted May 16, 2023. The copyright holder for this preprint (which was not certified by peer review) is the author/funder, who has granted bioRxiv a license to display the preprint in perpetuity. It is made available under aCC-BY-NC-ND 4.0 International license.

Figure 1

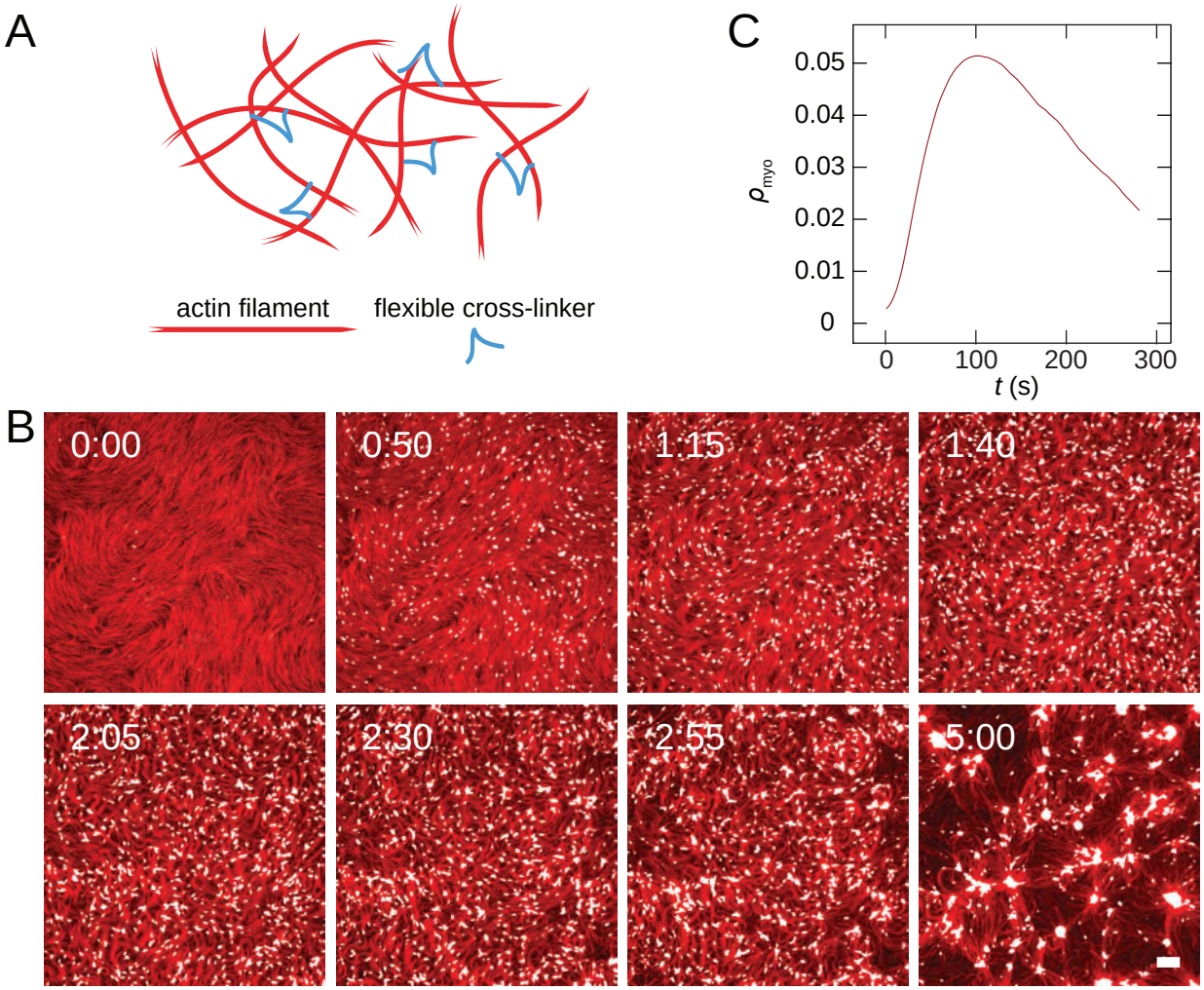

bioRxiv preprint doi: https://doi.org/10.1101/2023.05.15.540780; this version posted May 16, 2023. The copyright holder for this preprint (which was not certified by peer review) is the author/funder, who has granted bioRxiv a license to display the preprint in perpetuity. It is made available under aCC-BY-NC-ND 4.0 International license.

Figure 2

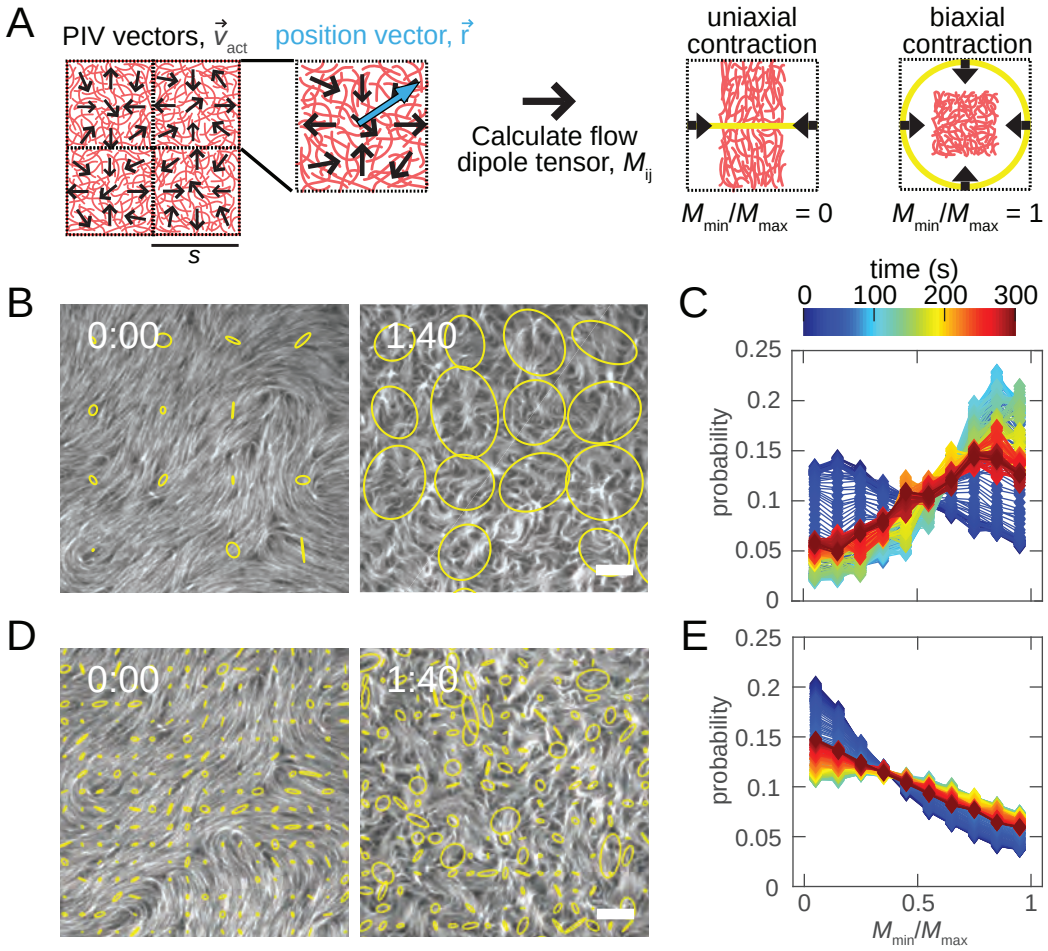

bioRxiv preprint doi: https://doi.org/10.1101/2023.05.15.540780; this version posted May 16, 2023. The copyright holder for this preprint (which was not certified by peer review) is the author/funder, who has granted bioRxiv a license to display the preprint in perpetuity. It is made available under aCC-BY-NC-ND 4.0 International license.

Figure 3

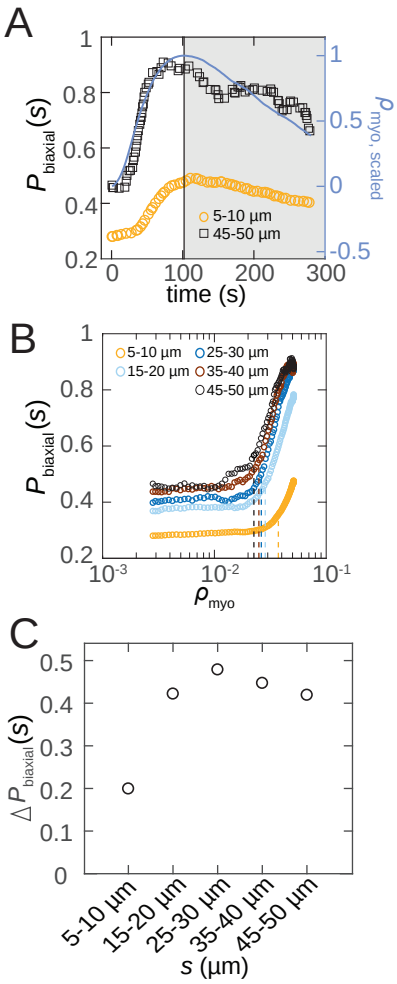

bioRxiv preprint doi: https://doi.org/10.1101/2023.05.15.540780; this version posted May 16, 2023. The copyright holder for this preprint (which was not certified by peer review) is the author/funder, who has granted bioRxiv a license to display the preprint in perpetuity. It is made available under aCC-BY-NC-ND 4.0 International license.

Figure 4

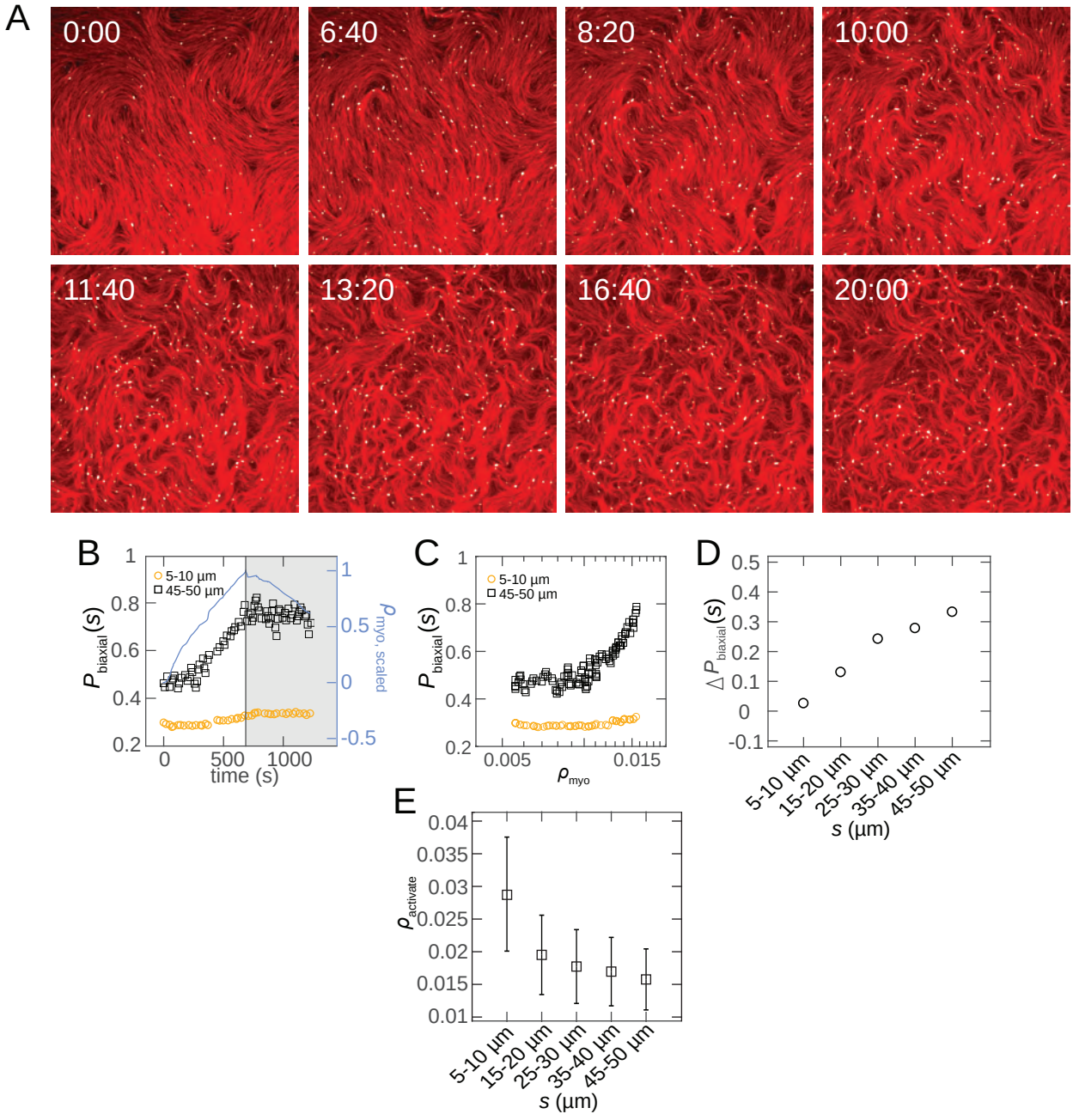

bioRxiv preprint doi: https://doi.org/10.1101/2023.05.15.540780; this version posted May 16, 2023. The copyright holder for this preprint (which was not certified by peer review) is the author/funder, who has granted bioRxiv a license to display the preprint in perpetuity. It is made available under aCC-BY-NC-ND 4.0 International license.

Figure 5

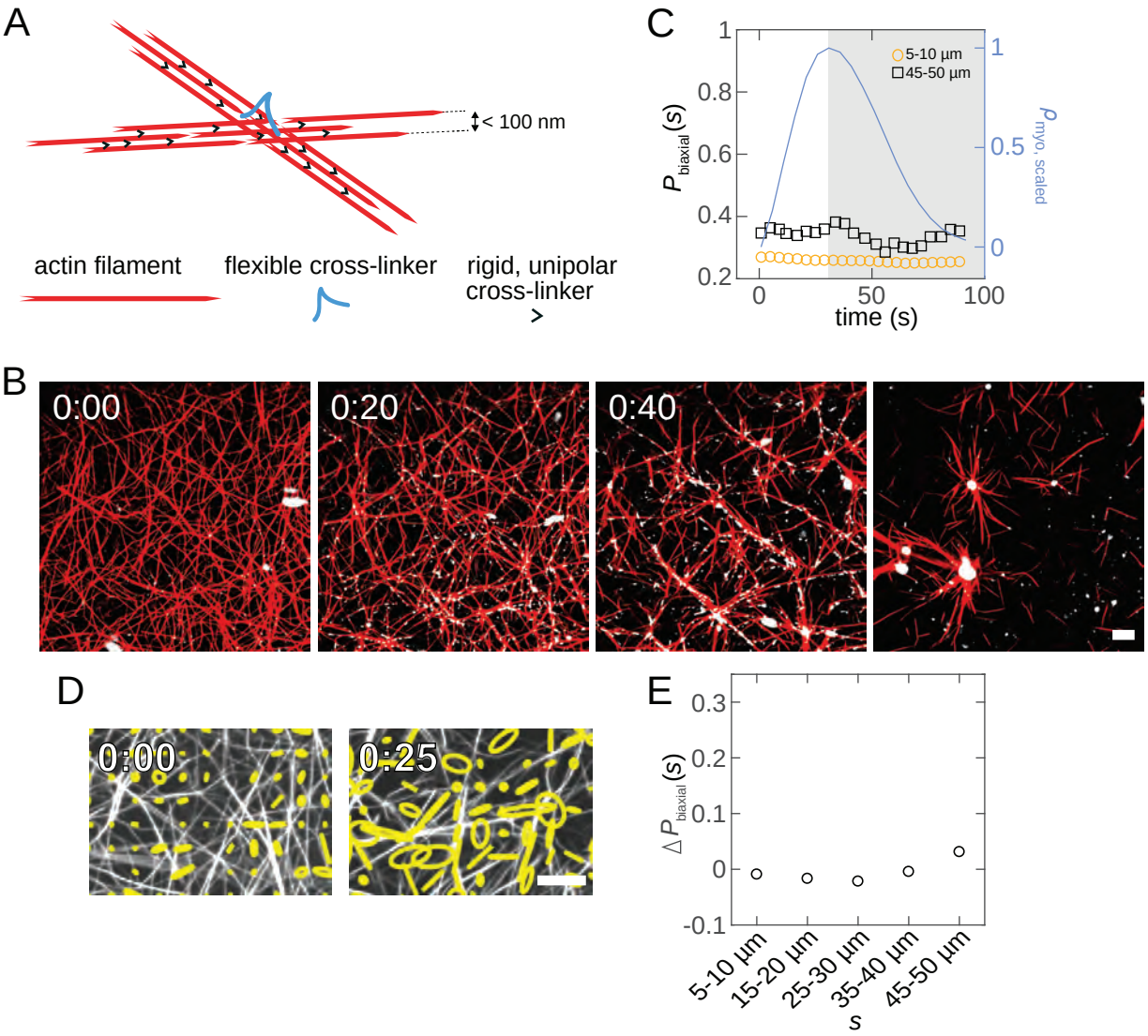

bioRxiv preprint doi: https://doi.org/10.1101/2023.05.15.540780; this version posted May 16, 2023. The copyright holder for this preprint (which was not certified by peer review) is the author/funder, who has granted bioRxiv a license to display the preprint in perpetuity. It is made available under aCC-BY-NC-ND 4.0 International license.

Figure 6